Nonhysteretic Vortex Magnetic Tunnel Junction Sensor with High Dynamic Reserve

Guanyang He[*], Yiou Zhang, and Gang Xiao[†]

Department of Physics, Brown University, Providence, Rhode Island 02912, USA

Multiple geometrical conditions for different magnetic vortex states to appear in micrometer-sized magnetic tunnel junctions (MTJs) are investigated in experiment and simulation. Both results match up well, providing clear images of vortex behaviors. We pattern a compact array of single-vortex MTJ elements and perform magnetotransport and noise measurements. This sensor features nonhysteretic behavior, a small size of 0.5×0.5 mm^2, a low normalized noise of 10^{-13} Hz^{-1}, a detectability of $18\,nT/\sqrt{Hz}$ at 1 Hz, and a large dynamic range of 100 Oe. Its 115 dB broad dynamic reserve and superior stability against temperature and environmental stray fields are ideally suited for magnetic sensing applications.

I. INTRODUCTION

Magnetic sensing technology is indispensable in vast areas of applications, such as information storage and processing, navigation, spintronic immunoassays, nondestructive evaluation, diagnosis of vehicular motion, and industrial metrology [1–3]. Among diverse types of magnetic sensors, the magnetic tunneling junction (MTJ) is noteworthy for its high sensitivity, ease of use, small size, low cost, and low power consumption, which can bridge the gap between sophisticated technology and practical applications [4]. For magnetic sensing applications, a linear and hysteresis-free response to a magnetic field is desired. Typical MTJs with ferromagnetic free layers tend to have appreciable magnetic hysteresis, lessening their sensitivity for small magnetic fields [5–7]. Reducing hysteresis has been a subject of intensive development, for which magnetic shape anisotropy or a biasing magnetic field have been utilized [8]. Nevertheless, finite hysteresis is still present, even under a large shape anisotropy [9,10], while magnetic field biasing unavoidably increases the complexity [5,8,11]. Another approach is to reduce the thickness of the MTJ free layer, so it becomes superparamagnetic [12–15]. Although hysteresis free, superparamagnetic MTJs are plagued with thermal instability and a small dynamic range [15].

Recently, a linearization strategy utilizing the vortex magnetization states has drawn attention [16–18]. Under small magnetic fields, ferromagnetic layers with lateral dimensions exceeding the exchange length could favor a vortex magnetization state over a single-domain state, where the magnetostatic energy dominates over the exchange energy [19,20]. Owing to its nontrivial topology, the vortex core undergoes reversible displacement, as long as the magnetic field is not so large that it annihilates the vortex. This leads to hysteresis-free behavior in the center of the magnetic transfer curve. Compared with other linearization strategies, a vortex-state MTJ completely eliminates hysteresis and shows good thermal stability. Since the vortex displacement is reversible, magnetic noise from the free layer is also found to be reduced [16,17]. Moreover, the flux-closed vortex state generates negligible stray fields and interferences on neighboring sensors or the entity to be sensed. As such magnetic coupling gives rise to additional noise [9], the vortex MTJ provides additional benefits to sensors consisting of an array of sensing elements.

Here, the nonhysteretic response and superior detectability in a compact array of MTJ elements in vortex states are reported. Contrary to previous work on vortex forms for circular MTJs with small diameters (submicron to 2 μm) [16,17,21], we extend the investigation to vortex states in MTJs with larger diameters (3–9 μm) and different aspect ratios. Combining magnetotransport measurements and micromagnetic simulations, different types of vortex states are identified. By integrating many vortex MTJs into one sensor unit, hysteresis-free behavior, a large dynamic range, and low intrinsic noise simultaneously are successfully achieved.

II. EXPERIMENTAL

The MTJ stacks in this work are all fabricated on thermally oxidized silicon wafers using a homemade high-vacuum magnetron sputtering system. The multilayer structure is Si/SiO$_2$/Ta(5)/Ru(30)/Ta(5)/Ru(2)/Ir$_{22}$Mn$_{78}$(18)/

———————
[*]guanyang_he@brown.edu
[†]Gang_Xiao@brown.edu

$Co_{50}Fe_{50}(3)/Ru(0.85)/Co_{40}Fe_{40}B_{20}(3)/Co_{50}Fe_{50}(0.5)/$ $MgO(2.9)/$free layer (FL)$/Ta(5)/Ru(10)$, where the numbers in parentheses represent the thickness of each layer in nanometers. The FL consists of $Co_{40}Fe_{40}B_{20}(0.4)/Co_{50}Fe_{50}(0.5)/Co_{40}Fe_{40}B_{20}(t)$, where t varies between 40 and 60 nm. The magnetic layer assembly below the MgO barrier serves as the reference layer. Standard photolithography and physical ion milling are used to pattern MTJ elements. Postgrowth thermal annealing is performed in a high-vacuum chamber at 280 °C for 1 h, under an external magnetic field of 0.5 T. More information can be found in our previous work [7]. Room-temperature magneto-transport measurements are performed on a probe station equipped with a pair of calibrated electromagnets, while temperature-dependent transport and noise measurements are performed in the Quantum Design® physical property measurement system (PPMS) combined with a home-made noise measurement system. A two-channel cross-correlation method is used in the noise measurements [22]. The noise measurement system has a bandwidth of 10 kHz and negligible background noise of $3\,nV/\sqrt{Hz}$. The sensitivity of the MTJ is measured by applying a modulating field ($\delta H = 0.25\,Oe$) at 1 Hz and measuring the voltage response. Previous work on tunneling magnetoresistance (TMR) sensors has found that such ac sensitivity measurement gives a more accurate estimation of the actual sensitivity [5–7].

III. RESULTS AND DISCUSSION

We pattern eight MTJs connected in series as one unit, where each MTJ has lateral dimensions $X \times Y$ in the x and y directions, with a free-layer parameter of $t = 40$ nm. In the postannealing process, the magnetic field is applied along the y direction, which sets the magnetic pinning direction. The conductance of these MTJs is measured as a function of a cycling magnetic field H_y applied along the y direction. The experimental results are shown in Figs. 1(a)–1(c), corresponding to different MTJs with dimensions of 5×5, 14×7, and $6 \times 10\ \mu m^2$, respectively. Based on such a MTJ geometry, MUMAX micromagnetic simulation is used to study the free-layer magnetization for different $X \times Y$ values. The simulation program determines the magnetization by minimizing the total magnetic energy. A saturation magnetization of 1.25×10^6 A/m, a Landau-Lifshitz damping coefficient of 4×10^{-3}, and an
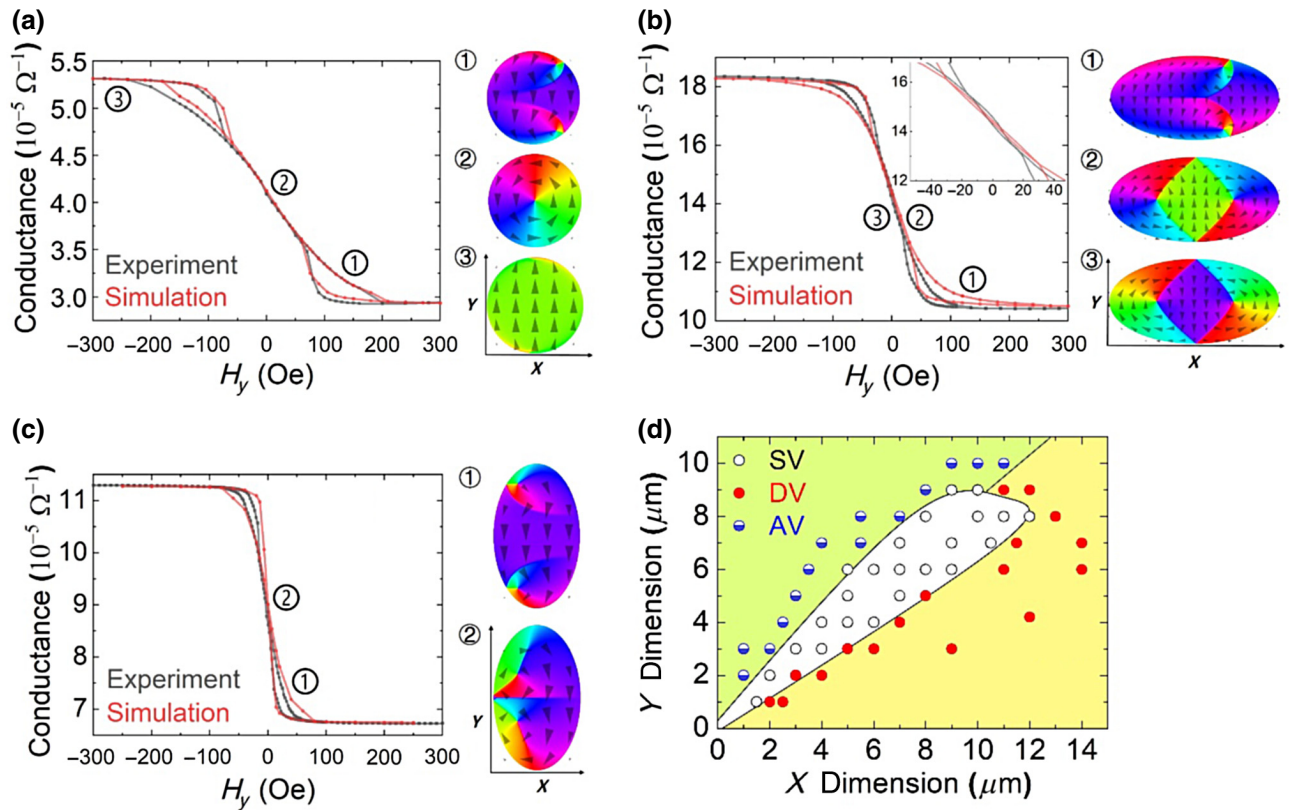

FIG. 1. Magnetic conductance transfer curve of MTJs in (a) single-vortex (SV) state ($X = 5\,\mu m$, $Y = 5\,\mu m$), (b) double-vortex (DV) state ($X = 14\,\mu m$, $Y = 7\,\mu m$), and (c) antivortex (AV) state ($X = 6\,\mu m$, $Y = 10\,\mu m$). Spin maps on the right side of each curve show the simulated magnetization at different positions of the transfer curve. In (b), an enlarged view shows a small hysteresis. (d) Summary of all simulation results, showing the vortex-state diagram over a wide range of X and Y dimensions.

annealing-induced uniaxial anisotropy of 866 J/m^3 in the y direction are used as the $Co_{40}Fe_{40}B_{20}$ parameters in the simulation [23–25]. The exchange stiffness of $Co_{40}Fe_{40}B_{20}$ in the literature varies from 10 to 20 pJ/m [26,27], and we use a value of 11 pJ/m, for which our simulations correspond well with experiments. From the simulated magnetization maps, we obtain the magnetization M_y along the y direction under multiple external magnetic fields H_y, which is related to the magnetoconductance by [28]

$$G = [(G_P + G_{AP}) + (G_P - G_{AP})M_y/M_S]/2, \quad (1)$$

where G_P (G_{AP}) is the conductance when free-layer magnetization is parallel (antiparallel), with respect to the reference (pinned) layer, and M_S is the saturation magnetization. The simulated conductance is presented together with the corresponding experimental results in Fig. 1. Also shown are the corresponding magnetization maps for the geometries considered.

These transfer conductance curves are characteristically different from each other, resulting from three types of vortex magnetization states: *SV*, *DV*, and *AV* states. In Fig. 1(a), with a moderate size and aspect ratio ($X/Y \sim 1$), the *SV* state is energetically favorable. Starting from a uniform magnetization for a saturation magnetic field in the y direction above 200 Oe, a buckling state initiates vortex nucleation (at position 1). When the field decreases below 75 Oe, the magnetic flux becomes completely closed. A single vortex is formed and its core position shifts in the x direction in response to external magnetic fields, giving a linear response range (at position 2). As the field goes to −200 Oe, the vortex core moves to the edge and finally opens up to return to a uniform magnetization (at position 3). Each configurational transition between these different magnetization maps is accompanied by an abrupt change in the susceptibility of the hysteresis loop. As the vortex core is topologically protected, magnetization is reversible and hysteresis free in a large range of external magnetic fields.

Similar configurational transitions apply to the formation of the *DV* state in Fig. 1(b). With an aspect ratio larger than one, i.e., $X/Y > 1$, the *DV* state is formed, which consists of two vortices. In such an oval-shaped free layer, the external magnetic field aligns the magnetization in the central region, while vortices exist near the edge due to the demagnetizing fields there. Because of the opposite chirality of two vortices, the interchange of their positions changes the overall vorticity. Therefore, such a magnetization topology has two possible maps (at positions 2 or 3). As the *DV* state lifts the energy degeneracy of vortex pairs with different vorticity, a small hysteresis around 2 Oe is observed.

When the aspect ratio is smaller than one, i.e., $X/Y < 1$, an antivortex (*AV*) is formed, as seen in Fig. 1(c). The *AV* state consists of two vortices and one antivortex. The

two vortices have the same chirality, so no new topological state can be created by interchanging their positions. Without any degeneracy, it shows no apparent hysteresis in the central part of the transfer curve. However, it stays in the buckling state for most of the field range and nucleates only at very small fields. As a result, its dynamic range is severely limited to below 20 Oe. Comparing the *AV* and *DV* states, the magnetic hysteresis can be reasonably attributed to the nondegeneracy of possible topological states.

Figure 1(d) is a summary of all simulation results, showing the phase diagram of the three vortex states, where three points are confirmed by experimental results, as given in Figs. 1(a)–1(c). Compared with *DV* and *AV* states, the *SV* state, extending over the white-shaded dimensional region, is completely hysteresis free and has a large dynamic range. Therefore, we focus on harnessing the *SV* state in the remaining part of this work.

Next, we pattern MTJ circular elements with a diameter of 5 μm into a compact array. The free-layer thickness is increased to $t = 60$ nm to further stabilize the vortex magnetization state. Each sensing unit is comprised of $48 \times 32 = 1536$ MTJ elements, with 48 MTJs in series as one row and 32 rows connected in parallel. Figure 2 is an optical micrograph of one such MTJ array, where some circular elements are visible in the magnified view. Any magnetic coupling between MTJ elements is suppressed due to the nature of the closed-vortex magnetization state. We choose a nearest-neighbor separation of 15 μm, which is much denser than our earlier work with other free-layer structures [9]. This increases the effective junction area and reduces low-frequency $1/f$ noise, while keeping the overall sensor size small to improve the spatial resolution. The area of one sensing unit is 0.5×0.5 mm^2.
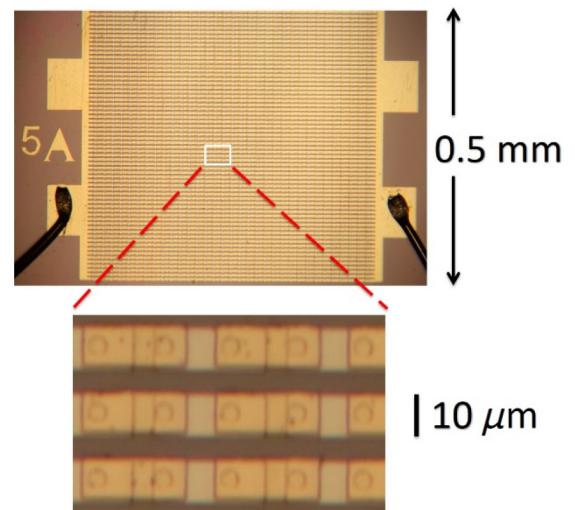

FIG. 2. Micrograph of the MTJ array sensor with an enlarged view of local MTJ circular elements.

Temperature-dependent transport and noise measurements are performed to characterize the sensing performance and temperature stability of this sensor array. From the transfer curves shown in Fig. 3(a), we can see that the *SV* state is preserved well under a large span of temperature from 250 to 350 K, and its nonhysteretic response is explicitly observed in the inset of Fig. 3(a). As shown in Fig. 3(b), the sensitivity of the sensor changes by only 5% over the same temperature range and 12% over a dynamic range of 100 Oe. The sensitivity of the *SV* MTJ depends on the ratio between the free-layer thickness and diameter, and our sensor with a smaller ratio shows much a higher sensitivity of 0.3%/Oe than that of previous results reported in the literature [17]. The inset of Fig. 3(b) shows the temperature dependence of the peak sensitivity, with a small temperature coefficient of only -400 ppm/K. The magnetic-field-dependent sensor noise is presented in Fig. 3(c). Overall, the voltage noise is low, with a calculated Hooge-like noise parameter, α, in the range of $10^{-9}\,\mu m^2$, except for abnormal peaks, where the vortex

core undergoes nucleation or annihilation. Such a special noise peak position is marked by label "1" throughout Fig. 3. Finally, in Fig. 3(d), we show the field detectability of this vortex sensor over the temperature range of 250 to 350 K and a field range of ± 400 Oe. A low detectability of $18\,nT/\sqrt{Hz}$ at 1 Hz is maintained over a large field range. The dynamic reserve (the ratio between the dynamic range and lowest detectable limit) calculated from data above is as high as 115 dB for a 1 Hz noise bandwidth of common data-acquisition devices.

To better understand the abnormal peaks of $1/f$ noise, we compare the noise spectrum of the vortex MTJ in the vortex nucleation region, position 1 in Fig. 3(a), and that in the vortex displacement region, position 2 in Fig. 3(a), as plotted in Fig. 4(a). While normal $1/f$ noise is observed when the vortex has already been formed, at the vortex nucleation region, there exists a big bump of Lorentzian shape, at low frequency with a few Hertz roll-off frequency. This is likely to be due to magnetization hopping of large activation energies [29]. The abnormal
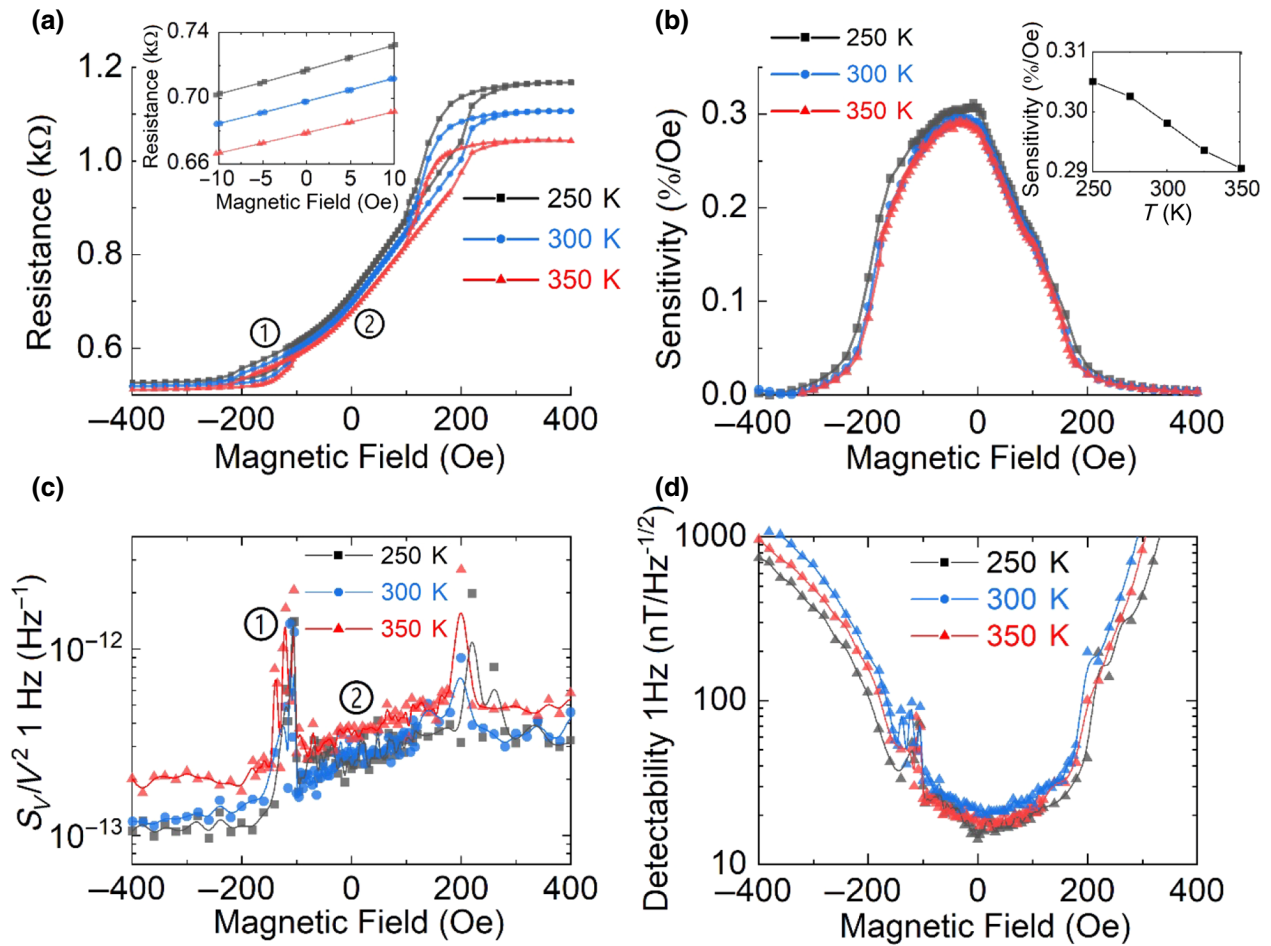

FIG. 3.   (a) Transfer curve of the MTJ array sensor shown in Fig. 2. Inset shows the linear hysteresis-free response of the sensor near zero field. (b) Sensitivity of the sensor versus field. Inset shows the peak sensitivity versus temperature. (c) Voltage noise at 1 Hz versus field. (d) Magnetic field detectability at 1 Hz versus field. Results are shown at $T = 250$, 300, and 350 K.
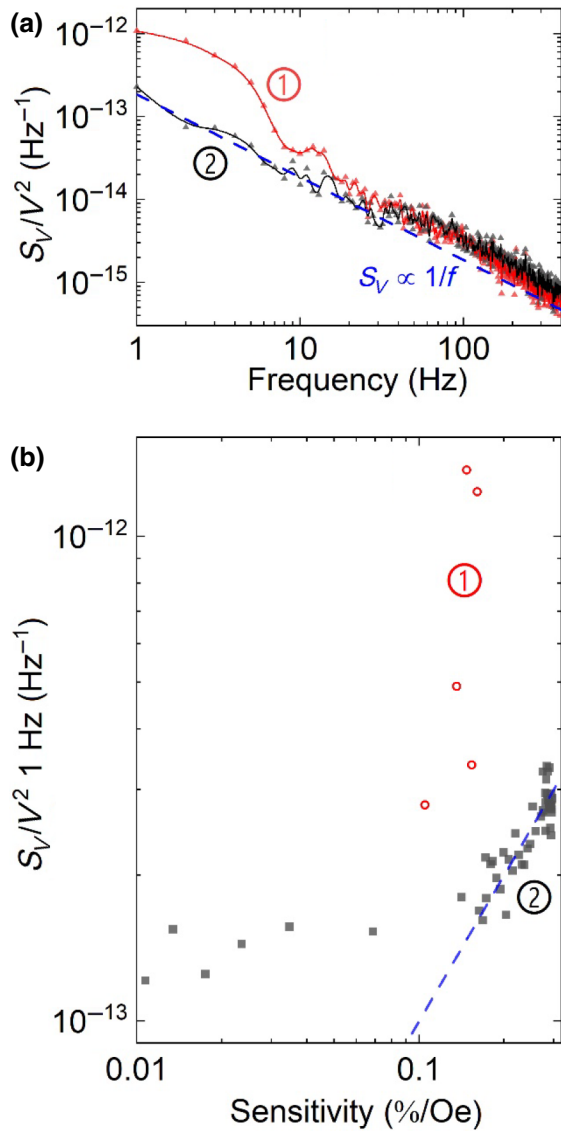
FIG. 4. (a) Normalized noise spectra at position 1 and position 2 in Fig. 3(a), with $1/f$ noise as the dashed line. (b) Scaling relation between voltage noise and sensitivity at position 1 and position 2 measured at 300 K. Linear dashed line is a guide to the eye.

dashed line. This implies that magnetic $1/f$ noise dominates when MTJ is in the high-sensitivity region, and its scaling with sensitivity can be well explained by the FD theorem. However, extra noise is observed near the vortex nucleation region, as an indication of the nonequilibrium phase-transition process.

IV. CONCLUSION

We study single-vortex, double-vortex, and antivortex states in MTJ free layers, for which simulation and experiment show good consistency. Single-vortex MTJs are further patterned into a high-density sensor array, which gives a nonhysteretic linear sensing range of 100 Oe. In this sensor, superior magnetic sensing performance is obtained, with a field detectability of $18\,\mathrm{nT}/\sqrt{\mathrm{Hz}}$ at 1 Hz, 115 dB dynamic reserve, together with high thermal stability and negligible dipolar stray field. The noise measurement shows a low normalized noise of $10^{-13}\,\mathrm{Hz}^{-1}$, and an interesting noise behavior relevant to the configurational transition during vortex nucleation. The results show that the vortex MTJ is a promising candidate for a high-density sensor array adequate for a broad range of applications, where hysteresis-free behavior, large dynamic range, and good detectability are desired.

noise behavior implies that, in the buckling state, domains of large magnetic moments can be significantly hopping due to a vortex configurational transition. Another way to understand it is by the scaling relation between noise and sensitivity. Using data measured at 300 K in Fig. 3, we plot this scaling relation in Fig. 4(b). Data of antiparallel MTJ states are neglected to avoid the noise contribution from the magnetic reversal of the reference layer [30]. From the fluctuation-dissipation (FD) theorem based on a quasiequilibrium assumption [31], low-frequency noise of the MTJ should scale linearly with MTJ sensitivity. Indeed, we find a linear scaling relation in the high-sensitivity region above 0.1%/Oe, where data points follow a linear

[1] K. Tsukada, Y. Haga, K. Morita, N. Song, K. Sakai, T. Kiwa, and W. Y. Cheng, Detection of inner corrosion of steel construction using magnetic resistance sensor and magnetic spectroscopy analysis, IEEE Trans. Magn. **52**, 1 (2016).

[2] M. H. Acuna, Space-based magnetometers, Rev. Sci. Instrum. **73**, 3717 (2002).

[3] M. Pannetier-Lecoeur, L. Parkkonen, N. Sergeeva-Chollet, H. Polovy, C. Fermon, and C. Fowley, Magnetocardiography with sensors based on giant magnetoresistance, Appl. Phys. Lett. **98**, 153705 (2011).

[4] P. P. Freitas, R. Ferreira, S. Cardoso, and F. Cardoso, Magnetoresistive sensors, J. Phys.: Condens Matter. **19**, 165221 (2007).

[5] D. Mazumdar, X. Y. Liu, B. D. Schrag, M. Carter, W. F. Shen, and G. Xiao, Low frequency noise in highly sensitive magnetic tunnel junctions with (001) MgO tunnel barrier, Appl. Phys. Lett. **91**, 033507 (2007).

[6] D. Mazumdar, W. F. Shen, X. Y. Liu, B. D. Schrag, M. Carter, and G. Xiao, Field sensing characteristics of

magnetic tunnel junctions with (001) MgO tunnel barrier, J. Appl. Phys. **103**, 113911 (2008).

[7] G. Y. He, Y. Zhang, L. J. Qian, G. Xiao, Q. Zhang, J. C. Santamarina, T. W. Patzek, and X. X. Zhang, Picotesla magnetic tunneling junction sensors integrated with double staged magnetic flux concentrators, Appl. Phys. Lett. **113**, 242401 (2018).

[8] G. Xiao, in *Handbook of Spin Transport and Magnetism*, edited by E. Y. Tsymbal, I. Zutic (CRC press, Taylor & Francis, Boca Raton, FL, USA, 2012).

[9] W. Z. Zhang, Q. Hao, and G. Xiao, Low-frequency noise in serial arrays of MgO-based magnetic tunnel junctions, Phys. Rev. B **84**, 094446 (2011).

[10] Z. Diao, E. R. Nowak, K. M. Haughey, and J. M. D. Coey, Nanoscale dissipation and magnetoresistive 1/f noise in spin valves, Phys. Rev. B **84**, 094412 (2011).

[11] S. Cardoso, D. C. Leitao, L. Gameiro, F. Cardoso, R. Ferreira, E. Paz, and P. P. Freitas, Magnetic tunnel junction sensors with pTesla sensitivity, Microsyst. Technol. **20**, 793 (2014).

[12] Y. Jang, C. Nam, J. Kim, B. Cho, Y. Cho, and T. Kim, Magnetic field sensing scheme using CoFeBâĽŢMgOâĽŢCoFeB tunneling junction with superparamagnetic CoFeB layer, Appl. Phys. Lett. **89**, 163119 (2006).

[13] W. F. Shen, B. D. Schrag, A. Girdhar, M. J. Carter, H. Sang, and G. Xiao, Effects of superparamagnetism in MgO based magnetic tunnel junctions, Phys. Rev. B **79**, 014418 (2009).

[14] J. W. Cao, Y. Liu, Y. Ren, F. L. Wei, and P. P. Freitas, Effect of annealing temperature on formation of superparamagnetism in CoFeB/MgO/CoFeB magnetic tunnel junctions, Appl. Surf. Sci. **314**, 443 (2014).

[15] Y. Zhang, G. Y. He, X. X. Zhang, and G. Xiao, Magnetotransport and electronic noise in superparamagnetic magnetic tunnel junctions, Appl. Phys. Lett. **115**, 022402 (2019).

[16] D. Suess, A. Bachleitner-Hofmann, A. Satz, H. Weitensfelder, C. Vogler, F. Bruckner, C. Abert, K. Prügl, J. Zimmer, and C. Huber, Topologically protected vortex structures to realize low-noise magnetic sensors, arXiv preprint arXiv:1712.07061 (2017).

[17] H. Weitensfelder, H. Brueckl, A. Satz, K. Pruegl, J. Zimmer, S. Luber, W. Raberg, C. Abert, F. Bruckner, and A. Bachleitner-Hofmann, Comparison of Sensitivity and Low-Frequency Noise Contributions in Giant-Magnetoresistive and Tunneling-Magnetoresistive Spin-Valve Sensors with a Vortex-State Free Layer, Phys. Rev. Appl. **10**, 054056 (2018).

[18] T. Wurft, W. Raberg, K. Prugl, A. Satz, G. Reiss, and H. Bruckl, The influence of edge inhomogeneities on vortex hysteresis curves in magnetic tunnel junctions, IEEE Trans. Magn. **53**, 1 (2017).

[19] K. Y. Guslienko, V. Novosad, Y. Otani, H. Shima, and K. Fukamichi, Magnetization reversal due to vortex nucleation, displacement, and annihilation in submicron ferromagnetic dot arrays, Phys. Rev. B **65**, 024414 (2001).

[20] T. Wurft, W. Raberg, K. Prügl, A. Satz, G. Reiss, and H. Brückl, Evolution of magnetic vortex formation in micronsized disks, Appl. Phys. Lett. **115**, 132407 (2019).

[21] T. Okuno, K. Shigeto, T. Ono, K. Mibu, and T. Shinjo, MFM study of magnetic vortex cores in circular permalloy dots: Behavior in external field, J. Magn. Magn. Mater. **240**, 1 (2002).

[22] M. Sampietro, L. Fasoli, and G. Ferrari, Spectrum analyzer with noise reduction by cross-correlation technique on two channels, Rev. Sci. Instrum. **70**, 2520 (1999).

[23] S. Y. Jang, C.-Y. You, S. H. Lim, and S. R. Lee, Annealing effects on the magnetic dead layer and saturation magnetization in unit structures relevant to a synthetic ferrimagnetic free structure, J. Appl. Phys. **109**, 013901 (2011).

[24] X. Liu, W. Zhang, M. J. Carter, and G. Xiao, Ferromagnetic resonance and damping properties of CoFeB thin films as free layers in MgO-based magnetic tunnel junctions, J. Appl. Phys. **110**, 033910 (2011).

[25] D. Garcia, J. L. Munoz, G. Kurlyandskaya, M. Vazquez, M. Ali, and M. R. J. Gibbs, Magnetic domains and transverse induced anisotropy in magnetically soft CoFeB amorphous thin films, IEEE Trans. Magn. **34**, 1153 (1998).

[26] N. Sato, R. M. White, and S. X. Wang, Effect of annealing on exchange stiffness of ultrathin CoFeB film with perpendicular magnetic anisotropy, Appl. Phys. Lett. **108**, 152405 (2016).

[27] T. Devolder, J. V. Kim, L. Nistor, R. Sousa, B. Rodmacq, and B. Dieny, Exchange stiffness in ultrathin perpendicularly magnetized CoFeB layers determined using the spectroscopy of electrically excited spin waves, J. Appl. Phys. **120**, 183902 (2016).

[28] J. C. Slonczewski, Conductance and exchange coupling of two ferromagnets separated by a tunneling barrier, Phys. Rev. B **39**, 6995 (1989).

[29] S. Ingvarsson, G. Xiao, S. Parkin, W. Gallagher, G. Grinstein, and R. Koch, Low-frequency Magnetic Noise in Micron-Scale Magnetic Tunnel Junctions, Phys. Rev. Lett. **85**, 3289 (2000).

[30] R. Stearrett, W. Wang, X. Kou, J. Feng, J. Coey, J. Xiao, and E. Nowak, Influence of exchange bias on magnetic losses in CoFeB/MgO/CoFeB tunnel junctions, Phys. Rev. B **86**, 014415 (2012).

[31] L. Jiang, E. Nowak, P. Scott, J. Johnson, J. Slaughter, J. Sun, and R. Dave, Low-frequency magnetic and resistance noise in magnetic tunnel junctions, Phys. Rev. B **69**, 054407 (2004).